ACS APPLIED MATERIALS & INTERFACES

Research Article

Cite This: ACS Appl. Mater. Interfaces 2019, 11, 38555−38567

www.acsami.org

Localized Free Radicals Burst Triggered by NIR-II Light for Augmented Low-Temperature Photothermal Therapy

Boshu Ouyang,[†,‡,¶] Funan Liu,[§,¶] Shuangrong Ruan,[‡] Yao Liu,[‡] Huishu Guo,[*,†] Zhengxu Cai,[∥] Xiangrong Yu,[*,⊥] Zhiqing Pang,[*,#] and Shun Shen[*,‡]

[†]Central Laboratory, First Affiliated Hospital, Institute (College) of Integrative Medicine, Dalian Medical University, Dalian 116021, China

[‡]The Institute for Translational Nanomedicine, Shanghai East Hospital, Tongji University School of Medicine, Shanghai 200120, China

[§]Department of Surgical Oncology, Affiliated Hospital 1, China Medical University, Shenyang 110001, China

[∥]Department of Neurology, Affiliated Hospital 1, Dalian Medical University, Dalian 116011, China

[⊥]Department of Radiology, Zhuhai Hospital, Zhuhai Peoples Hospital, Jinan University, Zhuhai 519000, China

[#]School of Pharmacy & Key Laboratory of Smart Drug Delivery, Fudan University, Shanghai 201203, China

Supporting Information

ABSTRACT: As a novel treatment modality of tumors, hypothermal hyperthermia employed relatively lower temperature (<45 °C) to damage cancer cells with mild toxicity to normal tissues. However, beyond that inducible heat resistance of tumor cells, the discounted therapeutic effect of low temperature hyperthermia was also ascribed to poor penetration of exogenous light stimulation and low accumulation of photothermal agents in tumor sites. Herein, we constructed a multifunctional in situ hydrogel of sodium alginate (ALG) via Ca^{2+} coordinated with ALG to encapsulate the photothermal agent of Ink and azo initiator of 2,2′-azobis[2-(2-imidazolin-2-yl)propane]dihydrochloride (AIPH) for effective tumor treatment. The designed ALG hydrogel was used to improve the therapeutic effect by increased accumulation of Ink and AIPH and avoid potential side-effects caused by the unexpected spread to the surrounding normal tissues. After injection, local low temperature stimulation was generated with near-infrared-II irradiation by a 1064 nm laser, triggering rapid decomposition of AIPH to produce alkyl radicals. The synergistic low temperature photothermal therapy and cytotoxic-free radicals enhanced the apoptosis of tumor cells via physical heat damage and lipid peroxidation. Thus, remarkable inhibition of tumor growth was observed in a subcutaneous colorectal cancer with negligible side effects. Furthermore, the formulation could also exert strong photoacoustic signals, which were utilized to monitor the stability of the composite hydrogel.

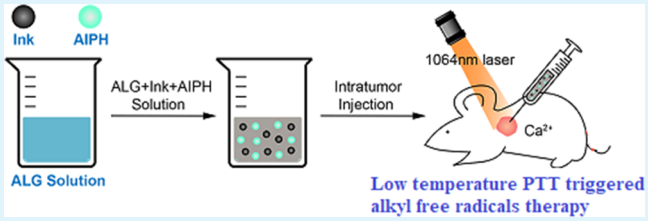

KEYWORDS: *free radicals, near infrared II photothermal therapy, ink, azo initiator, hydrogel*

INTRODUCTION

Photothermal therapy (PTT), which employs heat sensitizers to convert exogenous near-infrared (NIR) light to physical heat, is a promising technique of local tumor ablation with potential clinical application.[1−6] The generated high temperature in the local area by a minimally invasive way can effectively and rapidly eliminate tumors without systemic toxicity, compared with traditional surgical excision, chemotherapy, and radiotherapy.[7] However, the excessively high temperature of PTT (>50 °C) will inevitably cause damage to the surrounding normal tissues.[8−10] Considering the limited tissue penetration of NIR light, PTT is only effective for superficial or small tumors. In addition, once the tumors are too large or the lesions are deeper, the probability of complete ablation of tumors by PTT is significantly reduced, and the residual rate and recurrence rate are both increased.[11−13] Recently, low-temperature hyperthermia (<45 °C) by NIR-II laser irradiation has attracted great interests because of its good tolerance and safety to the surrounding tissues.[14−17] However, limited by the weak therapeutic effect of low-temperature hyperthermia, it usually requires multiple or continuous photothermal treatment.[18,19] In addition to inducible heat resistance of cancer cells,[20] applying this strategy requires high penetration and accumulation of photothermal agents in the tumor location. Therefore, in order to further improve the therapeutic effect of hypothermal hyperthermia, a combination with other therapies is often needed to precisely and effectively destroy tumors.[21,22]

Cytotoxic-free radicals are a class of active substances that can effectively induce necrosis or apoptosis of cancer cells.[23]

Received: August 21, 2019
Accepted: September 27, 2019
Published: September 27, 2019

DOI: 10.1021/acsami.9b15009
ACS Appl. Mater. Interfaces 2019, 11, 38555−38567

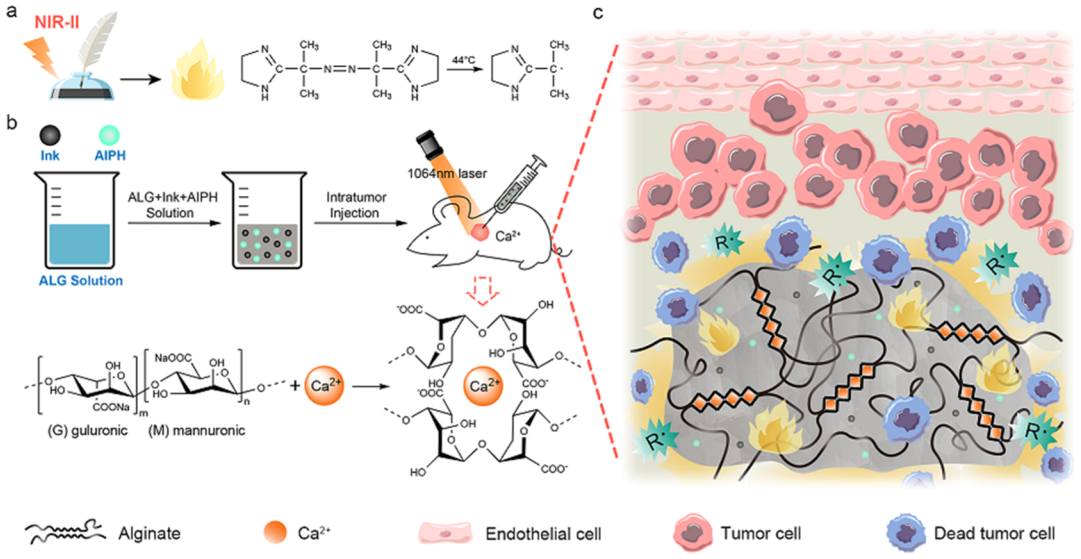

Figure 1. Schematic illustration of (a) 44 °C low-temperature produced by traditional Hu-Ink triggered AIPH to generate alkyl free radicals. (b) Syringeable AIPH + Ink + ALG hydrogel was intratumorally injected into tumor-bearing mice. The main principles of the transformation from ALG solution to hydrogel was performed. (c) Photosensitive AIPH + Ink + ALG hydrogel for localized tumor ablation.

Oxygen-related free radicals, such as reactive oxygen species (ROS), have been widely used in cancer radiotherapy,[11,24] chemotherapy,[25,26] photodynamic therapy,[27] and sonodynamic therapy.[28−30] It has been proved that cytotoxic-free radical-related therapeutic strategies can successfully apply to tumor therapy. However, the therapeutic effect of ROS is greatly compromised by the deep hypoxic microenvironment of tumors.[31,32] In view of the above limitations, carbon-centered highly reactive alkyl radicals have attracted much attention.[33] Because they are produced without oxygen supply, alkyl radicals are expected to overcome the deep hypoxic microenvironment of tumors and achieve complete ablation of tumors.[34−36] Thus, we intend to use the alkyl radical therapy strategy combined with hypothermal hyperthermia to maximize their advantages for cancer treatment.

Herein, low-temperature hyperthermia (<45 °C) was used to generate heat and then trigger the thermal degradation of azo initiator 2,2′-azobis[2-(2-imidazolin-2-yl)propane]-dihydrochloride (AIPH) to produce alkyl radicals for tumor therapy (Figure 1).[37] In order to achieve efficacious damage to deep-seated tumors, NIR-II laser light with stronger tissue penetration was chosen as an exogenous light stimulation.[38−41] At the same time, Hu Kaiwen Ink, a traditional Chinese Ink with good biocompatibility and eminent photothermal conversion efficiency was adopted as the corresponding NIR-II photothermal materials.[42−44] Ink was expected to produce local hypothermic stimulation by a 1064 nm laser to trigger the rapid decomposition of AIPH to generate alkyl radicals. The synergistic effect of low-temperature PTT and cytotoxic-free radicals induced apoptosis of tumor cells. However, there are difficulties in practical application, mainly because AIPH and Ink are both fluids, they are not easy to be fixed in tumor tissues after in situ injection, leading to the spread to the surrounding normal tissues.[45] In addition, AIPH is chemically unstable and easily degraded after exposure to the biological environment.[37] In order to enhance the stability of AIPH and the accumulation of AIPH and Ink in the tumor tissues, and to achieve the goal of multiple irradiation after single administration, sodium alginate (ALG), an excipient with excellent biocompatibility and degradability,[46] was selected as a carrier. Precursor liquids were obtained by simply mixing ALG with AIPH and Ink. They were injected into the tumors in a minimally invasive manner. ALG could rapidly react with Ca^{2+} and Mg^{2+} in tumor to form in situ hydrogel,[46,47] which encapsulated AIPH and Ink in the colloid to effectively immobilize drugs and avoid the premature degradation of AIPH. The 1064 nm laser was employed to irradiate the tumors. Ink-absorbed NIR-II light to generate mild heat, which could subsequently stimulate the thermal decomposition of AIPH to produce a large number of free radicals, and then synergistically damaged the tumor cells. Moreover, attributing to unique physical−chemical properties of Ink, the preparation could also produce strong photoacoustic (PA) signals,[48] which were utilized to monitor the stability of the ALG−AIPH−Ink system.

EXPERIMENTAL SECTION

Materials. All chemicals were of analytical grade and used without further purification. Hu-Ink was purchased from Anhui Jixi Hu Kaiwen Ink Factory, China. AIPH, ALG, and $CaCl_2$ were obtained from Aladdin Reagent Co. Ltd. (Shanghai, China). 2,2′-Azobis(3-ethylbenzothiazoline-6-sulfonic acid) (ABTS), methylene blue trihydrate (MB), and 2,7-dichlorofluorescin diacetate (DCFH-DA) were acquired from Sigma-Aldrich. A mitochondrial membrane potential assay kit with JC-1 was obtained from Beyotime Biotechnology Co. (Shanghai, China). Cell counting kit-8 (CCK-8), propidium iodide (PI), calcein acetoxymethyl ester (Calcein AM), and annexin-V-FITC/PI, DAPI were the products of KeyGen BioTech (Nanjing, China). Penicillin−streptomycin solution, Dulbecco's modified Eagle's medium, fetal bovine serum, and trypsin−ethylene diamine tetraacetic acid (EDTA, 0.05%) were obtained from Life Science (Gibco, Pittsburgh, USA). HCT116 and 293T cell lines were obtained from Chinese Academy of Sciences Cell Bank. Nude mice (6−8 weeks old) were acquired from Shanghai SLAC Lab Animal Co. Ltd. The animal experiment program was assessed and ratified by the Institutional Animal Care and Use Committee of Fudan University.

Synthesis and Characterization of Hydrogels. Inspissated Hu-Ink was primarily diluted into aqueous phase with a lower concentration, and the achieved Ink can be stockpiled for further use. The *z*-average diameter and zeta (ζ) potential of Ink were determined by a dynamic light scattering (DLS) detector (Zetasizer,

DOI: 10.1021/acsami.9b15009
ACS Appl. Mater. Interfaces 2019, 11, 38555−38567

Nano-ZS, Malvern, UK). By facilely mixing the Ink, AIPH, and ALG, we formed the injectable AIPH + Ink + ALG solution. Because of the constant concentration of Ca^{2+} in vivo, a certain density of ALG-mixed solution was employed to be gelation.

The stickiness of ALG hydrogel highly relies on the concentration of ALG. To verify the gelling properties of ALG, 60 μL ALG−Ink solution with elevated concentration of ALG (1, 5, 10, and 20 mg/mL) and a settled concentration of Ink (1 mg/mL) were injected into 8 mL Ca^{2+} (1.8 mmol/L) solution in a meter glass. Subsequently, free Ink and ALG−Ink contained 5 mg/mL ALG fluid were also compared. Photographs were taken at different times. The morphology of AIPH + Ink + ALG hydrogel was characterized with a scanning electron microscope (SEM) (Hitachi S4800). A spectrophotometer (PerkinElmer Lambda 750) was used to scan UV−vis−NIR spectra. Appearance change of drug released from the AIPH + Ink + ALG hydrogel in Ca^{2+}-containing solution was monitored. 100 μL of ALG (5 mg/mL) mixed with Ink (1 mg/mL) or AIPH (200 μg/mL) was injected into 4 mL Ca^{2+} liquor in a penicillin bottle, they were oscillated on a shaker for 24 h at 37 °C. The absorption spectrum of the supernatant was record by a UV−vis−NIR spectrophotometer.

Photothermal Effects Measurements. Briefly, different components of H_2O, ALG, Ink, ALG + Ink, and ALG + Ink + AIPH solutions were illuminated by a 1064 nm laser (0.5 W/cm^2) for 10 min, the temperature was recorded. Afterward, the photothermal effect of the ALG + AIPH + Ink hydrogel at varied Ink concentrations and the photothermal stabilities of Ink and hydrogel were monitored through a thermal infrared camera (InfraTec, VarioCAM hr research, Germany).

Generation of Free Radicals. The free radicals from hydrogel were measured by the generation of $ABTS^{+\bullet}$ which was produced by the chemical reaction between ABTS liquor (2 mg/mL, 0.2 mL) and AIPH (200 μg/mL, 0.2 mL). Instead of laser irradiation, the mixture was allowed to react at 37 or 44 °C for 2, 4, and 6 h. Then, the absorbance of attenuated $ABTS^{+\bullet}$ solution ranging from 400 to 900 nm was tested using a UV−vis spectrometer. In order to monitor $ABTS^{+\bullet}$ formation after 1064 nm laser illumination, ABTS liquor (2 mg/mL, 0.2 mL) were added with different formulations in a cup, respectively. The absorbance of diluted liquid was also recorded. Curves of absorbance of $ABTS^{+\bullet}$ at 736 nm in group AIPH, Ink, AIPH + Ink, and AIPH + Ink + ALG solution versus irradiation duration was tested by an automated microplate spectrophotometer (EpocH2, BioTek Instruments).

MB fading test, a classical colorimetric assay, was also used to verify the production of free radicals under an oxidative environment. In short, different formulas was mixed into an MB aqueous solution (MB 20 μg/mL). After illumination by a 1064 nm laser (0.5 W/cm^2, 10 min), the absorbance of above liquors at 644 nm was detected to determinate the decolorization of MB.[49]

Intracellular Free Radical Exploration. A DCFH-DA fluorescent probe was used to supervise the intracellular generation of free radicals. HCT116 cells were added with different formulations including AIPH (50 μg/mL), Ink (25 μg/mL), ALG (1 mg/mL) and 1064 nm laser (0.5 W/cm^2, 10 min). Subsequently, cells were rinsed twice with phosphate-buffered saline (PBS) and hatched with DCFH-DA (10 μM) for 30 min. Then, avoid light staining with DAPI for 5 min. The fluorescence signal of the sensitized DCFH-DA was imaged formation by a CLSM and semiquantified by ImageJ.

In Vitro Cytocompatibility and Cytotoxicity of Hydrogels. The compatibility of HCT116 cells and 293T cells was evaluated. Two cells were inoculated on 96-well plates (1×10^4 cells per well) and hatched with cell culture medium for 24 h, respectively. Afterward, cells were treated with Ink or AIPH at elevated concentrations for 24 h. After additional incubation, the medium was discarded and a standard CCK-8 was used to assess the cells viability.

The synergistic therapeutic effect in vitro of AIPH + Ink + ALG hydrogel contraposed HCT116 cells was also tested. After treatment, relative cell viability with elevated concentration of AIPH and Ink, with or without 1064 nm laser irradiation (0.5 W/cm^2, 10 min), was separately detected. Subsequently, cell viabilities of HCT116 cells incubated with AIPH + Ink + ALG hydrogel contained a constant concentration of ALG (1 mg/mL) and Ink (25 μg/mL) and elevated concentration of AIPH with or without 1064 nm laser irradiation for 10 min were also verified through the above methods.

Cell Apoptosis Assay. HCT116 cells were incubated in a 12-well plate for 24 h and treated with different formulations including AIPH (50 μg/mL), Ink (25 μg/mL), ALG (1 mg/mL), and laser (0.5 W/cm^2, 10 min). After 12 h cultivation, removed the culture medium by swilling with PBS for several times and cells were digested by trypsin containing no EDTA. Cells were following the test with flow cytometry to detect apoptosis cells stained with annexin V-FITC/PI.

The Calcein-AM/PI apoptosis detection assay was also utilized to qualitatively evaluate the cell apoptosis-inducing activity of different formulations in HCT116 cells. The samples were observed on a confocal microscope. Green and red fluorescence indicated living and dead cells, discretely. Average optical density inside cells can be measured by ImageJ software to provide semiquantitative data.

Mitochondrial Membrane Potential Monitor. HCT116 cells were seeded into confocal dishes for 24 h at 37 °C and incubated with different prescriptions containing AIPH (50 μg/mL), Ink (25 μg/mL), ALG (1 mg/mL), and laser (0.5 W/cm^2, 10 min). Finally, cells were dyed with JC-1 dyestuff for 30 min and the fluorescence signal was obtained by CLSM. The change of JC-1 indicator from red into green can facilely detect the decrease of cell membrane potential, and it is also an indicator of early apoptosis.

Lipidomics Analysis. HCT116 cells treated with Ink or AIPH + Ink containing a constant concentration of Ink (25 μg/mL) and AIPH (50 μg/mL) were collected. Whereafter cells were illuminated with a 1064 nm laser for 10 min. Six samples were set for each group. The lipid extraction process was as follows. (1) Transferring samples into 2 mL centrifuge tubes, adding 1 mL of MTBE solution (precooled at −20 °C) and five steel balls; (2) placing tubes into a high-flux tissue grinding device (60 Hz, 1.5 min); (3) supercentrifuging for 5 min with 12 000 rpm at room temperature and transferring the upper layer fluid into a fresh centrifugal tube. The samples were put in an air blast vacuum drying box; (4) dissociating samples with 200 μL isopropanol, 0.22 μm membrane filtration; (5) for the quality control specimens, taking 20 μL from each prepared sample to mix; (6) analyzing samples using liquid chromatography−mass spectrometry (LC−MS).[50−52]

In Vivo PA Imaging. Nude mice were divided into different groups at random and were subcutaneously injected with 60 μL of free Ink or ALG + Ink fluid (ALG 5 mg/mL, Ink 200 μg/mL), respectively. After gaseous anesthetization with 5% isoflurane, mice suffered from PA imaging and the signals obtained by a high-resolution PA imaging instrument (Vevo LAZR, A49, FujiFilm VisualSonics Inc.). Region of interests were trapped in the photo and their mean values of PA intensity were taken down for quantification analysis.

In Vivo Synergistic Cancer Therapy. HCT116 subcutaneous tumor models were set up to demonstrate the efficacy of different treatments. Thirty HCT116 tumor-bearing nude mice were sectionalized into six groups at random (n = 5). Tagged day 0 when tumor sizes achieved approximately 100 mm^3 and drugs were intratumor-injected. The nude mice received different treatments (injection volume: 50 μL, ALG: 5 mg/mL, Ink: 200 μg/mL, AIPH: 200 μg/mL, laser intensity: 1064 nm, 0.5 W/cm^2). Two hours later after injection. The groups were irradiated for 10 min and the second irradiation was given on the third day. Body weight and tumor volume were both recorded during administration. After the therapy for 15 days, all the mice suffered mercy killing. Tumor tissues were dissected to weigh and collected for photographing.

The stripped tumors were soaked with 4% paraformaldehyde for 48 h, embedded in paraffin, and made into 10 μm slices to study the apoptosis of tumor cells induced by different treatments. The sections were then subjected for histological analysis with H&E and TUNEL staining. Finally, the slices were visualized under a Leica DM inverted microscope.

DOI: 10.1021/acsami.9b15009
ACS Appl. Mater. Interfaces 2019, 11, 38555−38567

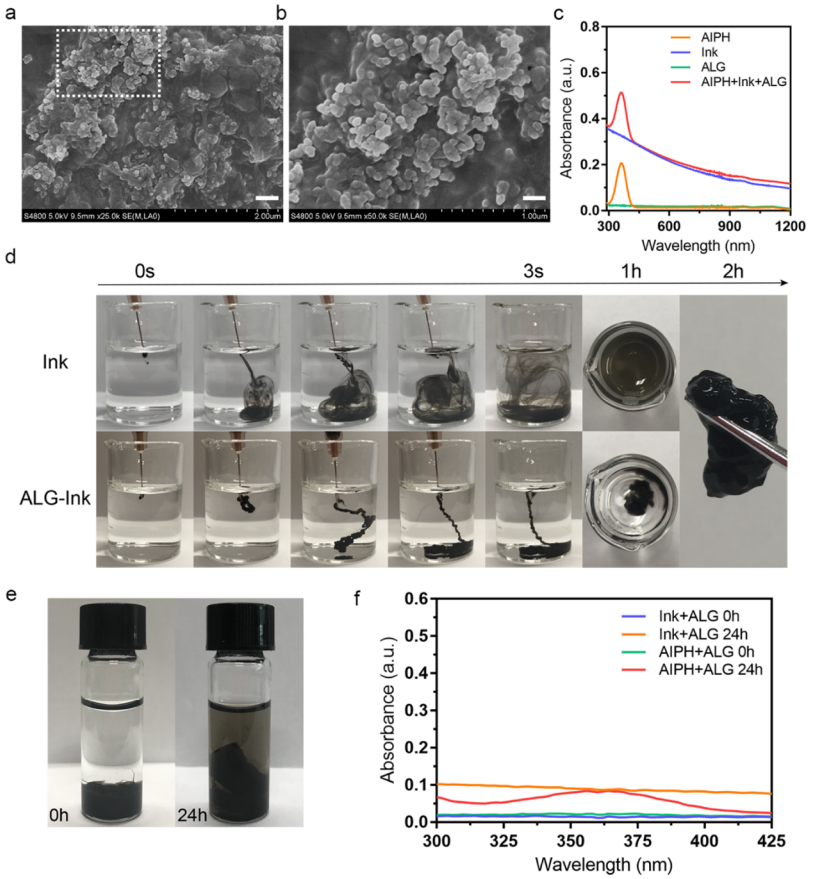

Figure 2. Structure evaluation and characterization of hydrogel. (a) SEM image of AIPH + Ink + ALG hydrogel at low. (b) High magnification. Scale bar of (a): 4 μm; scale bar of (b): 2 μm. (c) The UV−vis−NIR spectra of different formulas. (d) Photos of free Ink and ALG−Ink which contained 5 mg/mL alginate fluid both being injected into the Ca^{2+}-containing solution. (e) Appearance change of drug released from AIPH + Ink + ALG hydrogel in Ca^{2+}-containing solution. (f) UV−vis absorption spectra of free Ink or AIPH released from hydrogel which were oscillating on a shaker for 24 h at 37 °C.

Evaluation of Intratumor Oxidative Stress. DCFH-DA was chosen as a ROS probe to deliberate on intratumor oxidative stress in a subcutaneous tumor modal.[53] Tumor-bearing HCT116 mice suffered various treatments. After 12 h, all mice were euthanized. Tumors were gathered for cryosections and stained by DCFH-DA and DAPI. The field of vision were obtained by CLSM.

Toxicity Evaluation in Vivo. To assess the toxicity of hydrogels in vivo, the weight of mice was recorded every other day during the treatment. At 15 days, major organs including the heart, liver, spleen, lung, and kidney were dissected as mentioned above and served for H&E staining.

Statistical Analysis. Using unpaired student's *t*-test to appraise statistically significant discrepancies between two groups. One-way analysis of variance with Bonferroni tests for multiple group comparison. $*P < 0.05$, $**P < 0.01$, and $***P < 0.001$ indicated statistical difference and ns denoted no significant variation. All data were expressed as means ± standard deviation.

RESULTS AND DISCUSSION

Characterization of AIPH + Ink + ALG Hydrogel. The DLS and ζ-potential were used to characterize the Ink nanoparticles (NPs) with a hydrodynamic diameter of 162.7 nm and ζ potential of −16.3 mV (Figure S1). The results were consistent with previous reports.[42,43] Characterization of ALG−Ink hydrogel by SEM was performed. As shown in Figure 2a,b, numerous Ink nanospheres clustered on the hydrogel surface, which indicated that Ca^{2+} cross-linked ALG could effectively immobilize Ink NPs. The UV−vis absorption spectra of AIPH, Ink, ALG, and AIPH + Ink + ALG were tested, respectively (Figure 2c). ALG had almost no absorption in UV−vis, and AIPH had one strong absorption peak at ca. 360 nm. As with complex structures, the Ink NP solution had optical absorption in a wide range of 300−1200 nm, which ensured that it could generate the photothermal effect through NIR-II laser irradiation. The absorption spectrum of AIPH + Ink + ALG was almost the same as that of Ink, except that there was a strong AIPH absorption at ca. 360 nm, which further demonstrated that AIPH and Ink NPs were firmly encapsulated in Ca^{2+} cross-linked ALG. The gelation of ALG in Ca^{2+} solution with different concentrations was investigated. In our study, the concentration of Ca^{2+} with 1.8 mM was chosen to mimic the extracellular microenvironment in the living tissue.[54] The black Ink is not only a photothermal conversion agent, but also an ideal gelling indicator by naked eyes. As is shown in Figure S2, with the rise of ALG concentration, the gelling speed of ALG increased. When the ALG−Ink mixture (ALG: 1 mg/mL) was injected into the Ca^{2+} solution, it immediately gelled into a line and sank into the bottom of the cup. However, because of the weak gel, the black Ink−gel mixture spread to the whole bottom. When the ALG concentration was reached to 5 mg/mL or beyond, ALG gelled quickly just after being pushed out of the needle tip.[55] Within half an hour, the morphology of the gel hardly changed, let alone diffusion. In contrast, pure Ink was injected into the Ca^{2+} solution and then diffused into the whole solution (Figure

DOI: 10.1021/acsami.9b15009
ACS Appl. Mater. Interfaces 2019, 11, 38555−38567

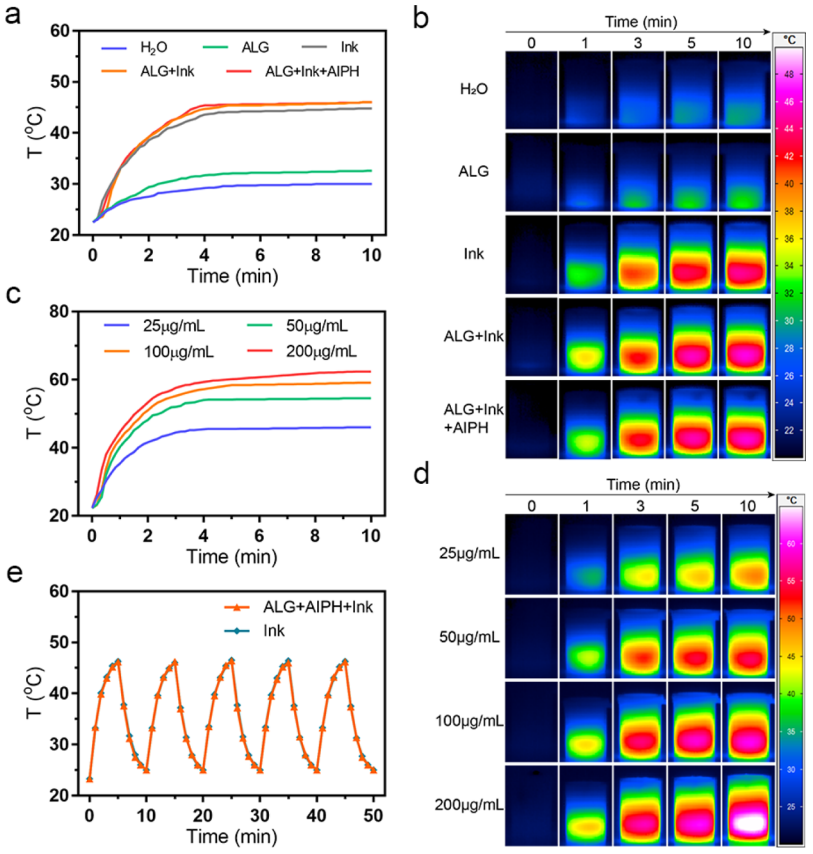

Figure 3. Photothermal-conversion property. (a) Photothermal curves of different groups irradiated by a 1064 nm laser (0.5 W/cm^2) for 10 min and (b) corresponding infrared thermal images. (c) Photothermal curves of ALG + AIPH + Ink hydrogel at different Ink concentrations upon a 1064 nm laser (0.5 W/cm^2) illumination and (d) homologous infrared thermal photos. (e) Photothermal stabilities of Ink and ALG + AIPH + Ink hydrogel after five times of laser irradiation.

2d). We chose a ALG concentration of 5 mg/mL for the further research. After 2 h, the whole ALG−Ink hydrogel was easily clamped up. Then, the release behaviors of Ink and AIPH from ALG + Ink + AIPH hydrogel were also investigated. As shown in Figure 2e, a little Ink was released from the hydrogel after 24 h shaking test. To further validate drug release, a UV−vis spectrometer was employed again to obtain the absorption spectrum of released Ink and AIPH. There was no UV−vis absorption at the initial stage due to no release of Ink and AIPH. After 24 h, typical absorption peaks of Ink and AIPH appeared (Figure 2f), showing that a little Ink and a few AIPH were released. The result indicated that the hydrogel had a noncompact structure, which was consistent with the reports that it is often used as a drug-sustained release carrier.[54,56]

Photothermal Effects of Pharmaceutical Compositions. After illumination, the slight temperature rise of water was measured. Similarly, the temperature of the ALG solution increased only about 6 °C. With the same Ink concentration, the temperature of Ink, ALG + Ink, and ALG + AIPH + Ink solutions increased significantly, and the rising temperature was basically identical, reaching about 44 °C (Figure 3a). An infrared thermal imaging camera was used to monitor temperature changes (Figure 3b). We also studied the heating effects with different Ink concentrations (Figure 3c,d). As the enhanced concentration of Ink, solution temperature increased after illumination, which indicated that the photothermal effect was dependent on the concentration of photothermal agents. In view of the low temperature PTT, we finally chose an Ink concentration of 25 μg/mL for a follow-up study. The photostability of Ink and its hydrogel complex were further investigated. As shown in Figure 3e, upon NIR-II illumination for 5 min, the Ink and its hydrogel complex solutions were naturally cooled at room temperature for another 5 min. Repeated this circulation five times. During the whole process, the temperature of the solution was persistently monitored by a thermal imaging camera. The results showed that there was no significant decline in the photothermal effect.

Extracellular and Intracellular Free-Radical Detection. The ability of AIPH to decompose into R$^\bullet$ under different conditions was investigated through detecting the concentration of ABTS$^{+\bullet}$ produced by the reaction of ABTS with free radicals. ABTS$^{+\bullet}$ has characteristic UV absorption peaks ranging from 400 to 900 nm. When ABTSs were incubated with AIPH at 37 and 44 °C, the formation of ABTS$^{+\bullet}$ was time dependent (Figure 4a). With the same incubation time, the absorbance of ABTS$^{+\bullet}$ was significantly higher at 44 °C than it was at 37 °C, which indicated that AIPH was decomposed faster at higher temperature. Subsequently, the formation abilities of ABTS$^{+\bullet}$ originated from four groups of Ink, AIPH, AIPH + Ink, and AIPH + Ink + ALG were compared by 1064 nm 0.5 W/cm^2 laser illumination for 20 min (Figure 4b,c). In order to optimize the irradiation time, we choose the absorbance of ABTS$^{+\bullet}$ at 736 nm as the ordinate and irradiation time as the abscissa to draw the curve (Figure 4c). The results showed that a mass of free radicals for AIPH + Ink and AIPH + Ink + ALG groups produced by 1064 nm laser irradiation reached their peaks at 10 min. In addition,

DOI: 10.1021/acsami.9b15009
ACS Appl. Mater. Interfaces 2019, 11, 38555−38567

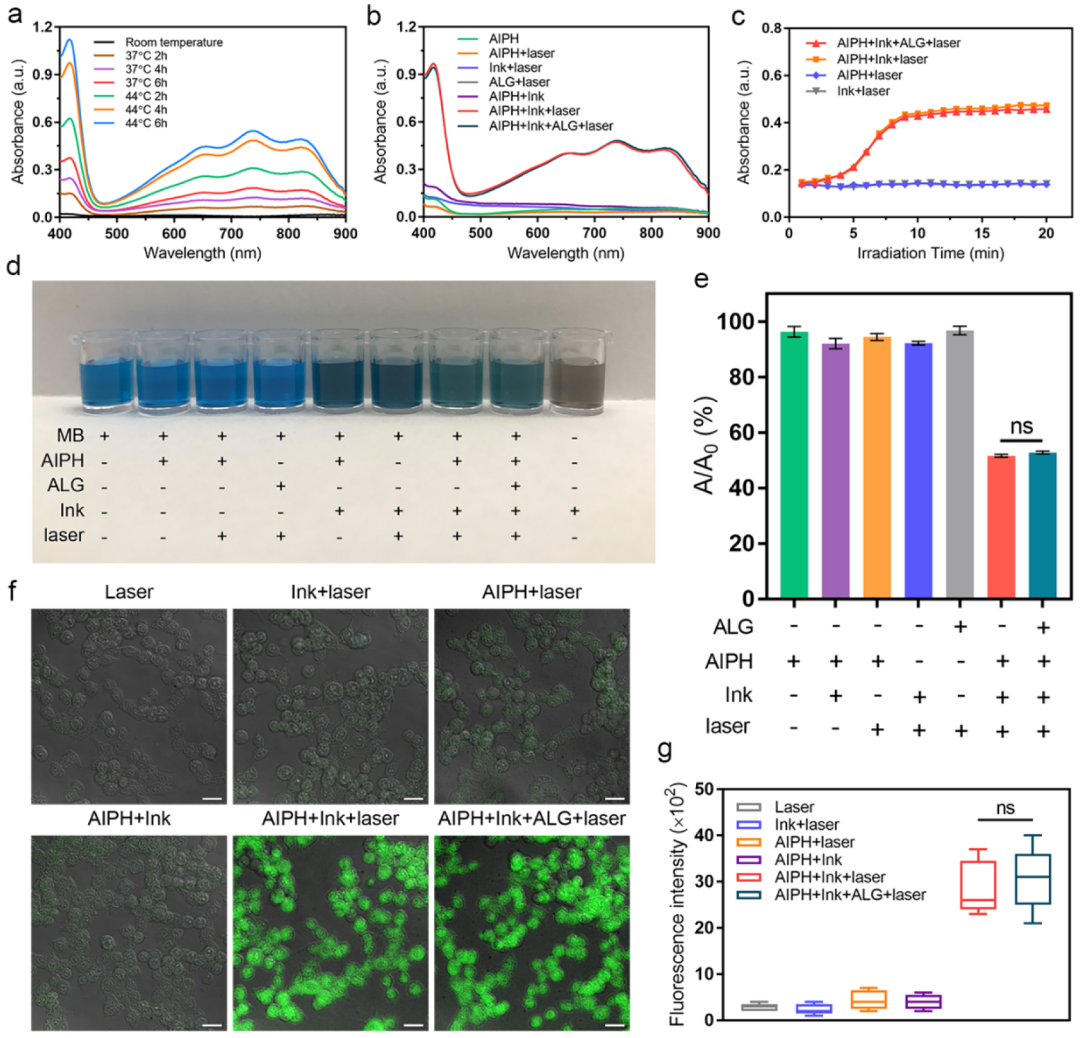

Figure 4. Detection of free radicals generated under 1064 nm NIR-II laser illumination. (a) Generation of $ABTS^{+\bullet}$ between ABTS and AIPH with different times and temperatures in a water bath. (b) UV−vis spectrum of $ABTS^{+\bullet}$ in solution with the administration of different formulations under irradiation (1064 nm, 0.5 W/cm^2). (c) Absorbance of $ABTS^{+\bullet}$ at 736 nm in AIPH, Ink, AIPH + Ink and AIPH + Ink + ALG solution vs irradiation duration. (d) Colorimetric analysis of the generation of free radicals for MB decolorization in different groups. (e) Relative absorbance of MB degradation at 644 nm triggered by free radicals under different conditions. (f) Determination of intracellular free radicals in HCT116 cells by a DCFH-DA probe. The cells were incubated with different formulations including AIPH (50 μg/mL), Ink (25 μg/mL), ALG (1 mg/mL), and 1064 nm laser (lighting for 10 min with a density of 0.5 W/cm^2). Scale bar: 20 μm. (g) Semiquantitative analysis of the expression of (f). ns denotes no significance.

AIPH produced free radicals mainly by heating Ink, while the addition of ALG had no significant effect on free radical production. Moreover, MB was also used to detect the formation of free radicals (Figure 4d,e). The color fading rates of AIPH + Ink + laser and AIPH + Ink + ALG + laser at 644 nm were 45.8 and 47.2% compared with untreated MB solution, respectively, which was mainly due to the formation of free radicals. In cells, $R^{\bullet}$ produced by heating AIPH could be oxidize to alkoxyl radical $RO^{\bullet}$, which induced ROS formation. Therefore, DCFH-DA was chosen as a fluorescent indicator to estimate the level of intracellular free radicals. As shown in Figure 4f, cells treated with AIPH + Ink and AIPH + Ink + ALG groups for irradiation time of 10 min showed bright green fluorescence, while the other four groups presented weak fluorescence signals. The fluorescence intensities were semi-quantitatively measured by ImageJ software (Figure 4g). The results indicated that both AIPH + Ink + laser and AIPH + Ink + ALG + laser groups could produce a large number of free radicals with no statistical difference.

In Vitro Cytotoxicity of AIPH + Ink + ALG Hydrogel. Then, we explored the potential of tumor therapy for gel complexes. As shown in Figure S3, two cell lines of HCT116 and 293T were selected to detect the cytotoxicity of Ink and AIPH by CCK-8. Ink has good biocompatibility. Even if the Ink concentration reached 400 μg/mL, almost no cytotoxicity was revealed. Few cytotoxicities was observed when the AIPH concentration rose to 200 μg/mL, which might be attributed to the slow decomposition of high-concentration AIPH to produce trace free radicals at 37 °C. Subsequently, HCT116 cells were cocultured with varying concentration of AIPH and Ink, respectively. Whether irradiated or not, AIPH alone did not cause significant cytotoxicity. However, the cell viability of Ink group was 73.6% when the Ink concentration enhanced to 25 μg/mL with laser illumination for 10 min (Figure 5a,b). Afterward, the killing effect of AIPH + Ink + ALG was evaluated. As shown in Figure 5c, with the increased concentration of AIPH, cell survival rate decreased, meanwhile Ink concentration holds 25 μg/mL and the temperature was

DOI: 10.1021/acsami.9b15009
ACS Appl. Mater. Interfaces 2019, 11, 38555−38567

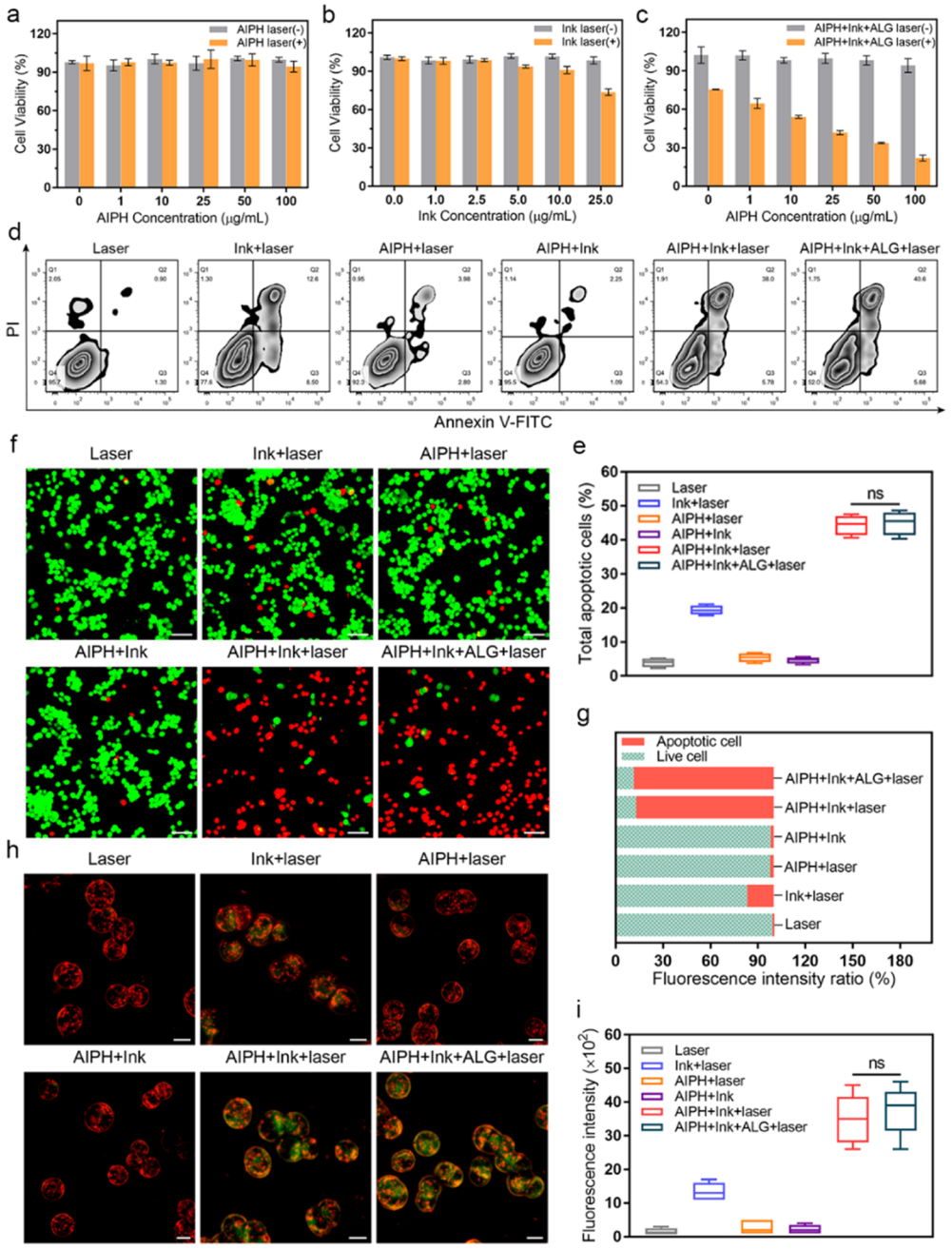

Figure 5. In vitro synergistic treatment of AIPH + Ink + ALG hydrogel against HCT116 cells. (a) Relative cell activity after dealing with raised concentration of AIPH with or without 1064 nm laser illumination for 10 min at the density of 0.5 W/cm^2. (b) Cell viability treated with varying concentrations of Ink with or without 1064 nm laser illumination for 10 min. (c) Relative cell viabilities of HCT116 cells conducted with AIPH + Ink + ALG hydrogel contained a constant concentration of ALG (1 mg/mL) and Ink (25 μg/mL) and elevated concentration of ALPH with 1064 nm laser irradiation or not for 10 min. (d) Flow cytometry apoptosis experiment based on annexin V-FITC/PI staining of HCT116 cells after incubation with different formulations including AIPH (50 μg/mL), Ink (25 μg/mL), ALG (1 mg/mL), and laser (0.5 W/cm^2, 10 min). (e) Semiquantitative analysis of the expression of (d). (f) Confocal photos of Calcein-AM/PI stained HCT116 cells after the treatments in (c). Scale bar: 50 μm. (g) Apoptosis ratios of differently treated cells was quantified. (h) JC-1 assay stained HCT116 cells after treatment as (c) for illustrating mitochondrial membrane potential loss. Scale bar: 10 μm. (i) Semiquantitative analysis of the fluorescence intensity of (h). ns denotes no significance.

controlled at 44 °C. When the AIPH concentration rose to 100 μg/mL, the cell survival rate was only 19.8%, indicating that the cytotoxicity of AIPH + Ink + ALG was related to the amount of free radical produced from the thermal decomposition of AIPH. Apoptosis was detected by annexin V-FITC/PI staining (Figure 5d,e). Both AIPH + Ink + laser and AIPH + Ink + ALG + laser groups showed significant cell apoptosis, with their early apoptosis and late apoptosis of about 44.38 and 45.0%, respectively. Calcein-AM/PI staining was further selected to observe the living and dead cells (Figure 5f,g). The results showed that only AIPH + Ink + laser and AIPH + Ink + ALG + laser groups presented strong red fluorescence, and the proportion of dead cells was ca. 87.08 and 88.48%, respectively. Apoptosis induces the reduction of mitochondrial

DOI: 10.1021/acsami.9b15009
ACS Appl. Mater. Interfaces 2019, 11, 38555−38567

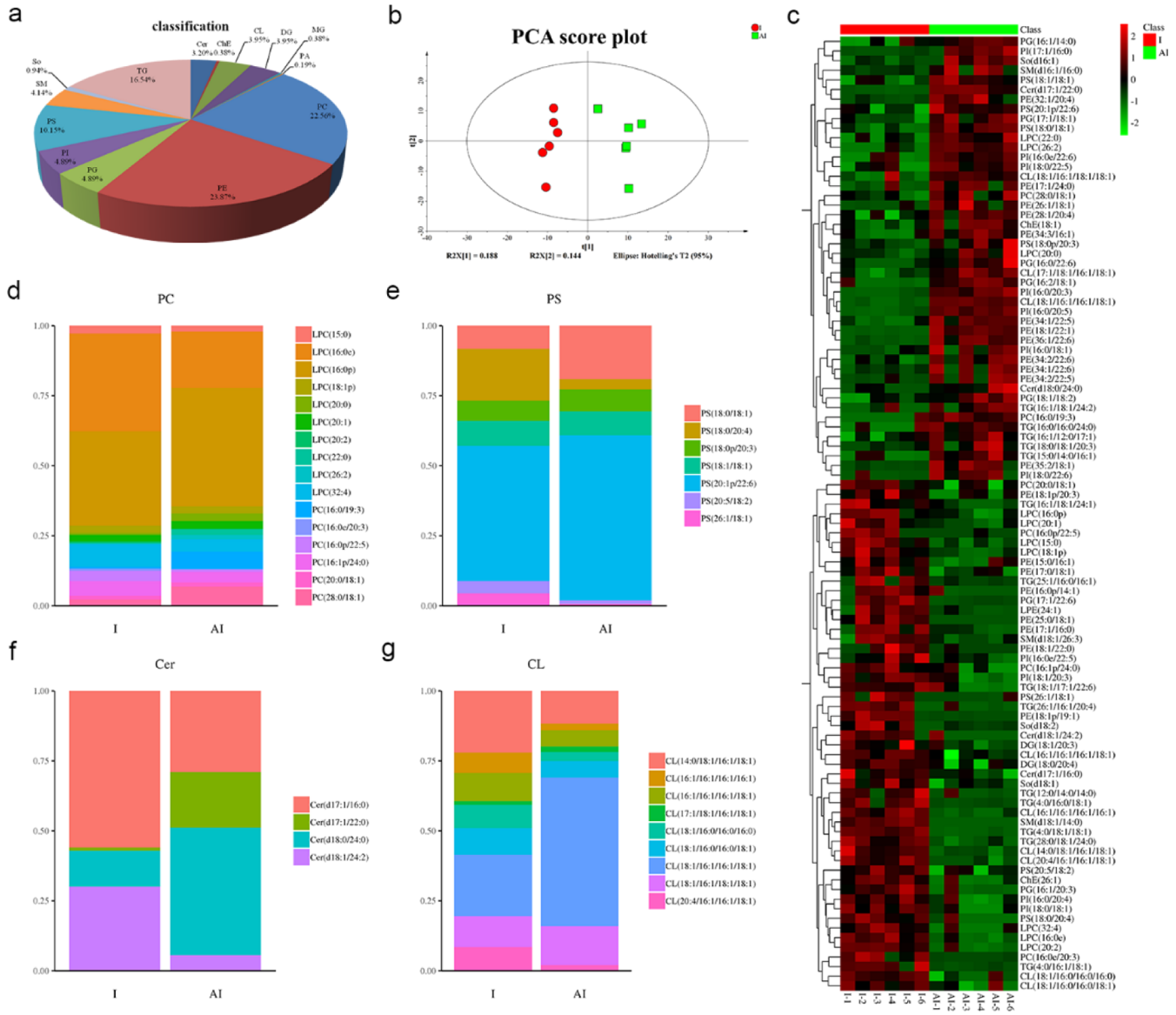

Figure 6. Lipidomics analysis. (a) Classification of the cell lipid by the biological process. (b) PCA score plot from the analysis of LC−MS spectra of HCT116 cells exposed to Ink with or without AIPH under 1064 nm laser. I: Ink; AI: AIPH + Ink. (AIPH: 50 μg/mL, Ink: 25 μg/mL, n = 6) (c) take the relative values of lipids under different experimental conditions (I or AI) as the metabolic level, hierarchical clustering analysis was conducted, and the results were presented by a heat map. The relative content is shown by color differences, with columns representing samples and rows representing lipids. (d−g) Lipids were screened for biomarkers, and the sublipid content in four main types of differential lipids (PC, PS, Cer, and CL) were statistically analyzed.

membrane potential, which can be a facile test by the transition of JC-1 from red fluorescence into green.[57] As shown in Figure 5h, I, the significant transitions were found in AIPH + Ink + laser and AIPH + Ink + ALG + laser groups. These results demonstrated that NIR-II low-temperature irradiation could trigger AIPH to produce free radicals through photothermal conversion of Ink, which induced cancer cell apoptosis.

Lipidomics Analysis. Free radicals are known to react with biological molecules including lipids, proteins, and DNA.[23] Lipids, as an important component of cell membranes, perform a vital role in maintaining cell structure and function, providing energy, and participating in signal transduction.[58] Many investigations indicated that polyunsaturated fatty acids (PUFAs) in lipid molecules are the main target of free radicals, which can reduce the production of lipid peroxidation products through the free radical chain reaction to cause cytotoxicity.[59,60] In this research, LC−MS was employed to compare the changes of cell lipid levels with or without free radicals between I (Ink + laser) and AI (AIPH + Ink + laser) groups. After data pretreatment, 532 lipid molecules were detected by searching the Lipid Map database, and the annotated lipids were classified into 14 categories according to the lipid chains and groups (Figure 6a): phosphatidic acids (0.19%), phosphatidylcholines (PC, 22.56%), phosphatidylethanolamines (23.87%), phosphatidylglycerols (4.89%), phosphatidylinositols (4.89%), phosphatidylserines (PS, 10.15%), triacylglycerols (16.54%), sphingomyelins (4.14%), sphingosines (0.94%), cardiolipins (CL, 3.95%), ceramides (Cer, 3.20%), cholesteryl esters (0.38%), diacylglycerols (DG, 3.95%), and monogalactosyl DGs (0.38%). Principal component analysis (PCA) was referenced to analyze the detected lipid molecules (Figure 6b). The PCA result showed that the

DOI: 10.1021/acsami.9b15009
ACS Appl. Mater. Interfaces 2019, 11, 38555−38567

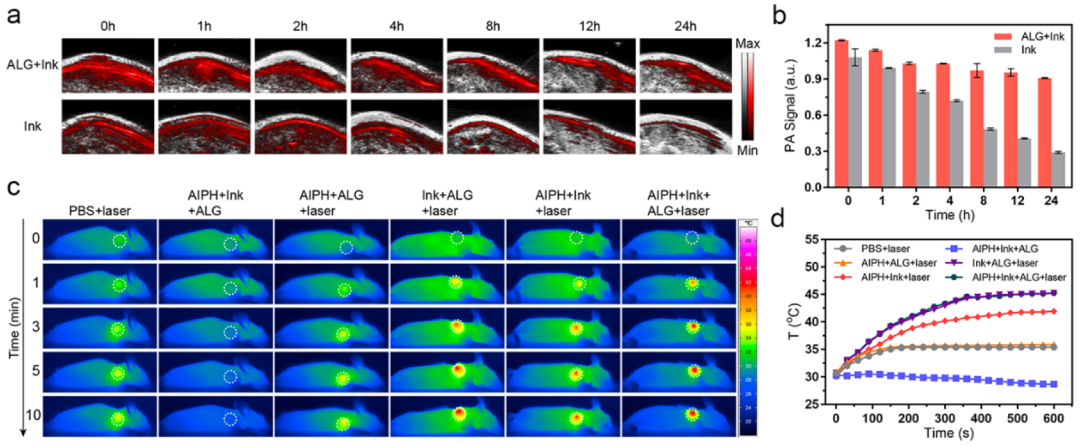

Figure 7. Locally sustained gelation and photothermal effect of hydrogel in vivo. (a) PA pictures and (b) PA signal intensity variation of mice after injection of the hydrogel or free Ink solution over time. (c) Infrared thermal images of different treatments with NIR laser irradiation (1064 nm, 0.5 W/cm^2) or not. (d) curve of tumor temperature rose with irradiation time.

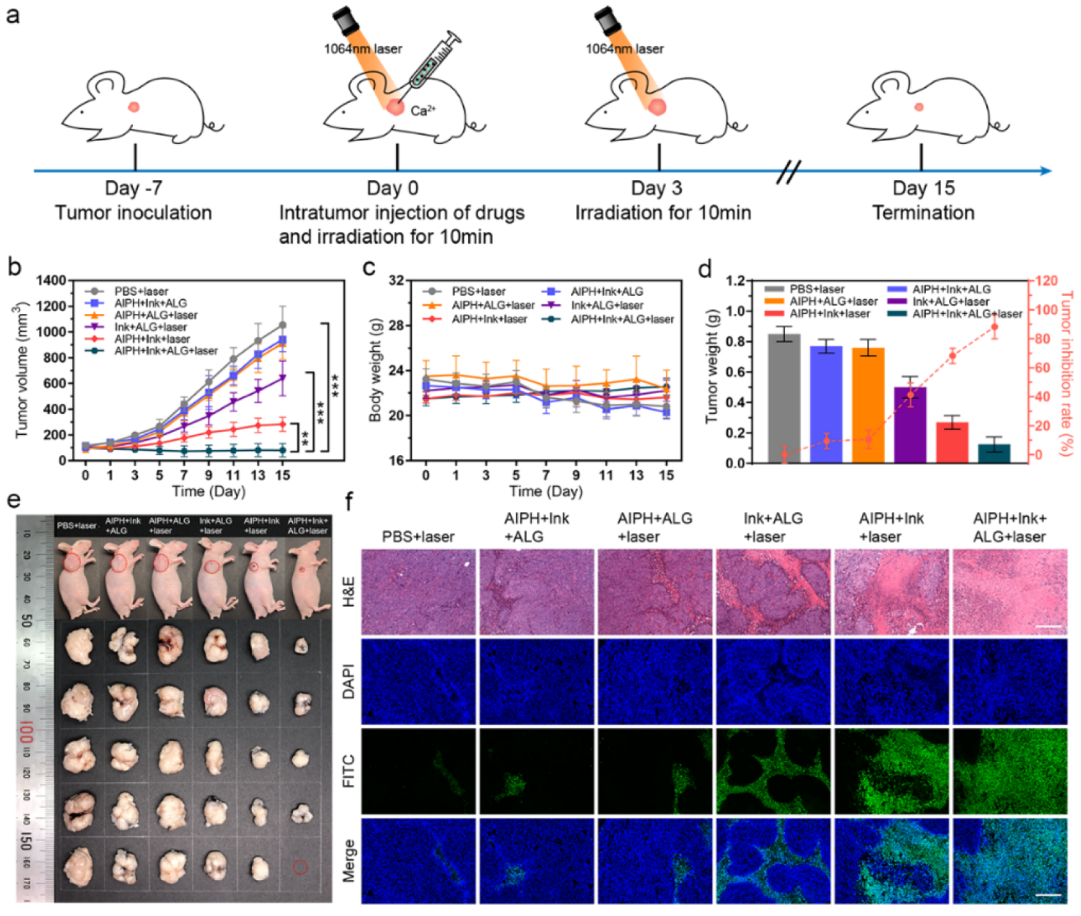

Figure 8. In vivo synergistic therapeutic effect of AIPH + Ink + ALG hydrogel. (a) Diagrammatic representation of the therapeutic experiment. (b) Tumor growth curves and (c) body weights of HCT116 tumor-bearing mice during the administration of different formulations. (d) Average tumor weight and tumor growth inhibition after various treatment. (e) Photographs of representative mice and tumors dissected from each group at 15th day once their treatment has finished. (f) H&E and TUNEL staining of tumor slicing at the end of treatment. Scale bar of H&E: 200 μm; scale bar of TUNEL: 100 μm. *P* values: $^*P < 0.05$; $^{**}P < 0.01$; $^{***}P < 0.001$.

AI group was clustered in the positive direction, while I as a control group was clustered in the negative direction. In order to further verify the difference between the two groups, partial least squares-discriminant analysis was implemented (Figure S4). Those results also showed that the two groups could be completely separated, which was consistent with the PCA result. Subsequently, 99 different lipids were screened by using the relevant differential screening conditions of *P*-value ≤ 0.05 and VIP ≥ 1 (Table S1). Standard variance *Z*-core was used to measure the relative content of lipids after free radical treatment at the same level (Figure S5). Meanwhile, the relative values of lipids under different experimental conditions

DOI: 10.1021/acsami.9b15009
ACS Appl. Mater. Interfaces 2019, 11, 38555−38567

were analyzed by hierarchical clustering, and the relative upregulation (red) or downregulation (green) of lipid concentration in the two groups were indicated by a thermogram (Figure 6c). Lipids of PUFAs containing unstable diallyl hydrogen atoms were highly susceptible to lipid peroxidation. The proportion of unsaturated fatty acids in subspecies lipids treated with or without alkyl radicals was compared. At the same time, the difference of subspecies lipids was displayed more intuitively by a box diagram. PC and PS containing arachidonic acid were easily oxidized. The result showed that the proportion of PUFAs such as LPC (20:2), LPC (32:4), PC (16:0e/20:3), PC (16:0p/22:5), PS (18:0/20:4), and PS (20:5/18:2) relatively diminished (Figures 6d,e and S6a–f). We also analyzed Cer and CL (Figures 6f,g and S6g,h). It was observed that the content of PUFAs in Cer (18:1/24:2) and CL (20:4/16:1/16:1/18:1) decreased as well. Finally, the correlation of different lipids was explored (Figure S7). The results showed that the lipid metabolites of similar types were distributed in the same cluster with similar trends. Therefore, it could be concluded that cytotoxicity was related to free radical-mediated lipid damage induced by AIPH heating.

Immobilization Ability of ALG Hydrogels. When mixed alginate solution was injected into tumor, the Ca^{2+} in vivo could react with ALG to form hydrogel in situ, which made drug encapsulation and slow release. In order to explore the immobilization ability of ALG hydrogels, we used Ink as a contrast agent to track the distribution of free Ink and ALG–Ink in vivo after injection (Figure 7a,b). The groups of 60 μL ALG–Ink solution (ALG 5 mg/mL, Ink 200 μg/mL) and 60 μL of free Ink solution (Ink 200 μg/mL) were subcutaneously injected into the mice, respectively. Owing to body fluid circulation, free Ink was gradually metabolized resulting in gradually weakening PA signals. After 24 h, the PA signal intensity decreased to 0.290. In contrast, in group ALG–Ink, the rate of Ink metabolism was slowed down because of the formation of gels in situ, and the PA signal intensity after 24 h was still 0.907. The results showed that the ALG–Ink hydrogel had a strong fixation ability. Therefore, it had enormous potential to enhance the efficacy of PTT and reduce the secondary action caused by rapid leakage of PTT drugs. To explore the photothermal effect of gel complexes in vivo, we used an infrared thermal imager to supervise the temperature variation of tumor-bearing mice in different treatments. As shown in Figure 7c,d, the temperature of the PBS + laser group increased to 35.4 °C by 1064 nm laser irradiation (0.5 W/cm^2, 10 min) after 2 h of intratumoral injection. In the AIPH + Ink + laser group, the temperature could only reach 41.8 °C due to the lack of ALG immobilization. In contrast, the temperature in the hydrogel-fixed Ink + ALG + laser and AIPH + Ink + ALG + laser groups increased rapidly to 44.8 °C and 44.9 °C, which could trigger the generation and release of free radicals. Twenty four hours after illumination, we removed the tumors from AIPH + Ink + ALG + laser and AIPH + Ink + laser to observe their cross sections (Figure S8). It can be seen intuitively that ALG could effectively reduce the leakage of Ink after forming gel in the tumor.

Evaluation of Intratumor Oxidative Stress. We further validated oxidative stress in the tumor tissue level. As shown in Figure S9, 12 h after treatment, the tumors were extracted for the frozen section using DCFH-DA as a probe. The staining results showed that AIPH + Ink + laser and AIPH + Ink + ALG + laser filled with strong DCF fluorescence signals, which were consistent with the cell results. It was proved that the free radicals produced by the thermal decomposition of AIPH could significantly enhance the oxidative response in tumors.

Antitumor Effect and Biocompatibility of the AIPH + Ink + ALG Hydrogel. We further studied the anticancer effect of HCT116 in vivo. Mice were randomly divided into six groups. When the tumors reached to 100 cm^3, the drugs were injected into the tumors and treated with laser irradiation on day 0 and 3 (Figure 8a). Changes in tumor volume and weight in mice were recorded (Figure 8b,c). The tumor volume of the AIPH + Ink + ALG + laser group was obviously smaller than that of the other five groups. On day 15, the tumors were removed to photograph and weigh (Figure 8d,e). It was clear to demonstrate that the therapeutic effects of PBS + laser, AIPH + Ink + ALG, and AIPH + ALG + laser groups could be neglected. The growth of tumors was partly inhibited in the Ink + ALG + laser group because of NIR-II low-temperature photothermal effect alone. The inhibition rate was 41.2% through calculation. The inhibition efficiencies of tumors growth in the AIPH + Ink + laser group and AIPH + Ink + ALG + laser group were significantly improved, which confirmed that the combination with the photothermal effect and free radicals could inhibit tumor multiplication more effectively. In particular, the therapy effect of the AIPH + Ink + ALG + laser group was the best with a tumor inhibition rate of 88.24% due to the good fixation ability of ALG on the drugs, such that the Ink and AIPH which remained in the tumor tissue could still work at the second laser irradiation. We further evaluated the tumor tissue with pathological sections (Figure 8f). H&E results displayed that the most obvious necrosis was in the AIPH + Ink + ALG + laser group. TUNEL immunofluorescence showed more overlaps of blue and green fluorescence, suggesting a mass of apoptotic cells. Finally, the biosafety was preliminarily assessed in vivo (Figures 8c and S10). There was no signal difference in body weight among the groups and no body weight loss caused by systemic toxicity. The tissues of the heart, liver, spleen, lung, and kidney were examined by H&E staining. There were no obvious inflammations and organ damages in the treatment groups compared with the PBS group.

CONCLUSIONS

A multifunctional injection gel with Ca^{2+}-coordinating sodium ALG as the carrier was constructed, encapsulating photothermal material of Ink and thermal-degradable azo initiator. Under the hypothermal hyperthermia, lots of free radicals were generated along with the thermal degradation of AIPH to synergistically kill tumors. The strategy has the superiority of enhanced stability, controlled release, and multimodal therapeutic effect. We confirmed the efficacy of synergistic therapy by inducing lipid oxidation of cancer cells in vitro and eradicating tumors in vivo. Simultaneously, the strong immobilization capacity of hydrogel was attested both in vitro and in vivo, which effectively promoted the high cumulation of agents in tumor and effectively prolongs the action time. Systematic toxicity evaluation also proved that the strategy had high biological safety and biocompatibility.

ASSOCIATED CONTENT

Supporting Information

The Supporting Information is available free of charge on the ACS Publications website at DOI: 10.1021/acsami.9b15009.

DOI: 10.1021/acsami.9b15009
ACS Appl. Mater. Interfaces 2019, 11, 38555–38567

Hydrodynamic diameter distribution and ζ potential of Ink, photographs of the ALG gelation, cell viability, lipidomics analysis, and DCFH-DA imaging and H&E images (PDF)

AUTHOR INFORMATION

Corresponding Authors

*E-mail: guohuishu1@126.com (H.G.).
*E-mail: yxr00125040@126.com (X.Y.).
*E-mail: zqpang@fudan.edu.cn (Z.P.).
*E-mail: nanocarries@gmail.com (S.S.).

ORCID

Xiangrong Yu: 0000-0003-2656-9847
Zhiqing Pang: 0000-0003-0228-904X
Shun Shen: 0000-0002-0184-6388

Author Contributions

¶B.O. and F.L. contributed equally to this work.

Notes

The authors declare no competing financial interest.

ACKNOWLEDGMENTS

We gratefully acknowledge financial support from the National Natural Science Foundation of China (81671815, 81673727, 81701684, 81273919).

REFERENCES

(1) Cheng, L.; Wang, C.; Feng, L.; Yang, K.; Liu, Z. Functional Nanomaterials for Phototherapies of Cancer. *Chem. Rev.* **2014**, *114*, 10869−10939.

(2) Shanmugam, V.; Selvakumar, S.; Yeh, C.-S. Near-Infrared Light-Responsive Nanomaterials in Cancer Therapeutics. *Chem. Soc. Rev.* **2014**, *43*, 6254−6287.

(3) Yang, K.; Xu, H.; Cheng, L.; Sun, C.; Wang, J.; Liu, Z. In Vitro and In Vivo Near-Infrared Photothermal Therapy of Cancer Using Polypyrrole Organic Nanoparticles. *Adv. Mater.* **2012**, *24*, 5586−5592.

(4) Huang, P.; Lin, J.; Li, W.; Rong, P.; Wang, Z.; Wang, S.; Wang, X.; Sun, X.; Aronova, M.; Niu, G.; Leapman, R. D.; Nie, Z.; Chen, X. Biodegradable Gold Nanovesicles with an Ultrastrong Plasmonic Coupling Effect for Photoacoustic Imaging and Photothermal Therapy. *Angew. Chem., Int. Ed.* **2013**, *52*, 13958−13964.

(5) Wang, X.; Li, H.; Liu, X.; Tian, Y.; Guo, H.; Jiang, T.; Luo, Z.; Jin, K.; Kuai, X.; Liu, Y.; Pang, Z.; Yang, W.; Shen, S. Enhanced Photothermal Therapy of Biomimetic Polypyrrole Nanoparticles through Improving Blood Flow Perfusion. *Biomaterials* **2017**, *143*, 130−141.

(6) Yao, J.; Liu, Y.; Wang, J.; Jiang, Q.; She, D.; Guo, H.; Sun, N.; Pang, Z.; Deng, C.; Yang, W.; Shen, S. On-Demand CO Release for Amplification of Chemotherapy by MOF Functionalized Magnetic Carbon Nanoparticles with NIR Irradiation. *Biomaterials* **2019**, *195*, 51−62.

(7) Liu, H.; Chen, D.; Li, L.; Liu, T.; Tan, L.; Wu, X.; Tang, F. Multifunctional Gold Nanoshells on Silica Nanorattles: A Platform for the Combination of Photothermal Therapy and Chemotherapy with Low Systemic Toxicity. *Angew. Chem., Int. Ed.* **2011**, *50*, 891−895.

(8) Yoo, D.; Jeong, H.; Noh, S.-H.; Lee, J.-H.; Cheon, J. Magnetically Triggered Dual Functional Nanoparticles for Resistance-Free Apoptotic Hyperthermia. *Angew. Chem., Int. Ed.* **2013**, *52*, 13047−13051.

(9) Chen, W.-H.; Luo, G.-F.; Lei, Q.; Hong, S.; Qiu, W.-X.; Liu, L.-H.; Cheng, S.-X.; Zhang, X.-Z. Overcoming the Heat Endurance of Tumor Cells by Interfering with the Anaerobic Glycolysis Metabolism for Improved Photothermal Therapy. *ACS Nano* **2017**, *11*, 1419−1431.

(10) Diederich, C. J. Thermal Ablation and High-Temperature Thermal Therapy: Overview of Technology and Clinical Implementation. *Int. J. Hyperthermia* **2011**, *21*, 745−753.

(11) Zhang, C.; Zhao, K.; Bu, W.; Ni, D.; Liu, Y.; Feng, J.; Shi, J. Marriage of Scintillator and Semiconductor for Synchronous Radiotherapy and Deep Photodynamic Therapy with Diminished Oxygen Dependence. *Angew. Chem., Int. Ed.* **2015**, *54*, 1770−1774.

(12) Liu, Y.; Liu, Y.; Bu, W.; Cheng, C.; Zuo, C.; Xiao, Q.; Sun, Y.; Ni, D.; Zhang, C.; Liu, J.; Shi, J. Hypoxia Induced by Upconversion-Based Photodynamic Therapy: Towards Highly Effective Synergistic Bioreductive Therapy in Tumors. *Angew. Chem., Int. Ed.* **2015**, *54*, 8105−8109.

(13) Tsai, M.-F.; Chang, S.-H. G.; Cheng, F.-Y.; Shanmugam, V.; Cheng, Y.-S.; Su, C.-H.; Yeh, C.-S. Au Nanorod Design as Light-Absorber in the First and Second Biological Near-Infrared Windows for in Vivo Photothermal Therapy. *ACS Nano* **2013**, *7*, 5330−5342.

(14) Yang, Y.; Zhu, W.; Dong, Z.; Chao, Y.; Xu, L.; Chen, M.; Liu, Z. 1D Coordination Polymer Nanofibers for Low-Temperature Photothermal Therapy. *Adv. Mater.* **2017**, *29*, 1703588.

(15) Hu, Y.; Chi, C.; Wang, S.; Wang, L.; Liang, P.; Liu, F.; Shang, W.; Wang, W.; Zhang, F.; Li, S.; Shen, H.; Yu, X.; Liu, H.; Tian, J. A Comparative Study of Clinical Intervention and Interventional Photothermal Therapy for Pancreatic Cancer. *Adv. Mater.* **2017**, *29*, 1700448.

(16) Gao, G.; Jiang, Y.-W.; Jia, H.-R.; Sun, W.; Guo, Y.; Yu, X.-W.; Liu, X.; Wu, F.-G. From Perinuclear to Intranuclear Localization: A Cell-penetrating Peptide Modification Strategy to Modulate Cancer Cell Migration under Mild Laser Irradiation and Improve Photothermal Therapeutic Performance. *Biomaterials* **2019**, *223*, 119443.

(17) Hua, X.-W.; Bao, Y.-W.; Zeng, J.; Wu, F.-G. Ultrasmall All-In-One Nanodots Formed via Carbon Dot-Mediated and Albumin-Based Synthesis: Multimodal Imaging-Guided and Mild Laser-Enhanced Cancer Therapy. *ACS Appl. Mater. Interfaces* **2018**, *10*, 42077−42087.

(18) Chen, W.; Ouyang, J.; Liu, H.; Chen, M.; Zeng, K.; Sheng, J.; Liu, Z.; Han, Y.; Wang, L.; Li, J.; Deng, L.; Liu, Y.-N.; Guo, S. Black Phosphorus Nanosheet-Based Drug Delivery System for Synergistic Photodynamic/Photothermal/Chemotherapy of Cancer. *Adv. Mater.* **2017**, *29*, 1603864.

(19) Gao, G.; Jiang, Y. W.; Sun, W.; Guo, Y.; Jia, H. R.; Yu, X. W.; Pan, G. Y.; Wu, F. G. Molecular Targeting-Mediated Mild-Temperature Photothermal Therapy with a Smart Albumin-Based Nanodrug. *Small* **2019**, *15*, 1900501.

(20) Wu, J.; Bremner, D. H.; Niu, S.; Shi, M.; Wang, H.; Tang, R.; Zhu, L.-M. Chemodrug-Gated Biodegradable Hollow Mesoporous Organosilica Nanotheranostics for Multimodal Imaging-Guided Low-Temperature Photothermal Therapy/Chemotherapy of Cancer. *ACS Appl. Mater. Interfaces* **2018**, *10*, 42115−42126.

(21) Liu, T.; Wang, C.; Gu, X.; Gong, H.; Cheng, L.; Shi, X.; Feng, L.; Sun, B.; Liu, Z. Drug Delivery with PEGylated MoS_2 Nano-sheets for Combined Photothermal and Chemotherapy of Cancer. *Adv. Mater.* **2014**, *26*, 3433−3440.

(22) Zheng, M.; Yue, C.; Ma, Y.; Gong, P.; Zhao, P.; Zheng, C.; Sheng, Z.; Zhang, P.; Wang, Z.; Cai, L. Single-Step Assembly of DOX/ICG Loaded Lipid−Polymer Nanoparticles for Highly Effective Chemo-photothermal Combination Therapy. *ACS Nano* **2013**, *7*, 2056−2067.

(23) Daum, S.; Reshetnikov, M. S. V.; Sisa, M.; Dumych, T.; Lootsik, M. D.; Bilyy, R.; Bila, E.; Janko, C.; Alexiou, C.; Herrmann, M.; Sellner, L.; Mokhir, A. Lysosome-Targeting Amplifiers of Reactive Oxygen Species as Anticancer Prodrugs. *Angew. Chem., Int. Ed.* **2017**, *56*, 15545−15549.

(24) Liu, T.-I.; Yang, Y.-C.; Chiang, W.-H.; Hung, C.-K.; Tsai, Y.-C.; Chiang, C.-S.; Lo, C.-L.; Chiu, H.-C. Radiotherapy-Controllable Chemotherapy from Reactive Oxygen Species-Responsive Polymeric Nanoparticles for Effective Local Dual Modality Treatment of Malignant Tumors. *Biomacromolecules* **2018**, *19*, 3825−3839.

(25) Lin, Q.; Bao, C.; Yang, Y.; Liang, Q.; Zhang, D.; Cheng, S.; Zhu, L. Highly Discriminating Photorelease of Anticancer Drugs

DOI: 10.1021/acsami.9b15009
ACS Appl. Mater. Interfaces 2019, 11, 38555−38567

Based on Hypoxia Activatable Phototrigger Conjugated Chitosan Nanoparticles. *Adv. Mater.* **2013**, *25*, 1981−1986.
(26) Ma, P.; Xiao, H.; Yu, C.; Liu, J.; Cheng, Z.; Song, H.; Zhang, X.; Li, C.; Wang, J.; Gu, Z.; Lin, J. Enhanced Cisplatin Chemotherapy by Iron Oxide Nanocarrier-Mediated Generation of Highly Toxic Reactive Oxygen Species. *Nano Lett.* **2017**, *17*, 928−937.
(27) Xiang, H.; Chen, H.; Tham, H. P.; Phua, S. Z. F.; Liu, J.-G.; Zhao, Y. Cyclometalated Iridium(III)-Complex-Based Micelles for Glutathione-Responsive Targeted Chemotherapy and Photodynamic Therapy. *ACS Appl. Mater. Interfaces* **2017**, *9*, 27553−27562.
(28) Huang, P.; Qian, X.; Chen, Y.; Yu, L.; Lin, H.; Wang, L.; Zhu, Y.; Shi, J. Metalloporphyrin-Encapsulated Biodegradable Nanosystems for Highly Efficient Magnetic Resonance Imaging-Guided Sonodynamic Cancer Therapy. *J. Am. Chem. Soc.* **2017**, *139*, 1275−1284.
(29) Han, X.; Huang, J.; Jing, X.; Yang, D.; Lin, H.; Wang, Z.; Li, P.; Chen, Y. Oxygen-Deficient Black Titania for Synergistic/Enhanced Sonodynamic and Photoinduced Cancer Therapy at Near Infrared-II Biowindow. *ACS Nano* **2018**, *12*, 4545−4555.
(30) Dai, C.; Zhang, S.; Liu, Z.; Wu, R.; Chen, Y. Two-Dimensional Graphene Augments Nanosonosensitized Sonocatalytic Tumor Eradication. *ACS Nano* **2017**, *11*, 9467−9480.
(31) Martin Brown, J.; Wilson, W. R. Exploiting Tumour Hypoxia in Cancer Treatment. *Nat. Rev. Cancer* **2004**, *4*, 437−447.
(32) Vaupel, P.; Höckel, M.; Mayer, A. Detection and Characterization of Tumor Hypoxia Using pO2 Histography. *Antioxid. Redox Signaling* **2007**, *9*, 1221−1236.
(33) Chen, Z.-H.; Saito, Y.; Yoshida, Y.; Niki, E. Effect of Oxygen Concentration On Free Radical-Induced Cytotoxicity. *Biosci., Biotechnol., Biochem.* **2008**, *72*, 1491−1497.
(34) Shen, S.; Zhu, C.; Huo, D.; Yang, M.; Xue, J.; Xia, Y. A Hybrid Nanomaterial for the Controlled Generation of Free Radicals and Oxidative Destruction of Hypoxic Cancer Cells. *Angew. Chem., Int. Ed.* **2017**, *56*, 8801−8804.
(35) Wang, X.-Q.; Gao, F.; Zhang, X.-Z. Initiator-Loaded Gold Nanocages as a Light-Induced Free-Radical Generator for Cancer Therapy. *Angew. Chem., Int. Ed.* **2017**, *56*, 9029−9033.
(36) Xiang, H.; Lin, H.; Yu, L.; Chen, Y. Hypoxia-Irrelevant Photonic Thermodynamic Cancer Nanomedicine. *ACS Nano* **2019**, *13*, 2223−2235.
(37) Liao, W.; Ning, Z.; Chen, L.; Wei, Q.; Yuan, E.; Yang, J.; Ren, J. Intracellular Antioxidant Detoxifying Effects of Diosmetin on 2,2-Azobis(2-amidinopropane) Dihydrochloride (AAPH)-Induced Oxidative Stress through Inhibition of Reactive Oxygen Species Generation. *J. Agric. Food Chem.* **2014**, *62*, 8648−8654.
(38) Lin, H.; Gao, S.; Dai, C.; Chen, Y.; Shi, J. A Two-Dimensional Biodegradable Niobium Carbide (MXene) for Photothermal Tumor Eradication in NIR-I and NIR-II Biowindows. *J. Am. Chem. Soc.* **2017**, *139*, 16235−16247.
(39) Wang, X.; Ma, Y.; Sheng, X.; Wang, Y.; Xu, H. Ultrathin Polypyrrole Nanosheets via Space-Confined Synthesis for Efficient Photothermal Therapy in the Second Near-Infrared Window. *Nano Lett.* **2018**, *18*, 2217−2225.
(40) Li, B.; Lu, L.; Zhao, M.; Lei, Z.; Zhang, F. An Efficient 1064 Nm NIR-II Excitation Fluorescent Molecular Dye for Deep-Tissue High-Resolution Dynamic Bioimaging. *Angew. Chem., Int. Ed.* **2018**, *57*, 7483−7487.
(41) Xu, G.; Yan, Q.; Lv, X.; Zhu, Y.; Xin, K.; Shi, B.; Wang, R.; Chen, J.; Gao, W.; Shi, P.; Fan, C.; Zhao, C.; Tian, H. Imaging of Colorectal Cancers Using Activatable Nanoprobes with Second Near-Infrared Window Emission. *Angew. Chem., Int. Ed.* **2018**, *57*, 3626−3630.
(42) Liu, Q.-C.; Li, L.; Xu, J.-J.; Chang, Z.-W.; Xu, D.; Yin, Y.-B.; Yang, X.-Y.; Liu, T.; Jiang, Y.-S.; Yan, J.-M.; Zhang, X.-B. Flexible and Foldable Li−O_2 Battery Based on Paper-Ink Cathode. *Adv. Mater.* **2015**, *27*, 8095−8101.
(43) Wang, S.; Cao, Y.; Zhang, Q.; Peng, H.; Liang, L.; Li, Q.; Shen, S.; Tuerdi, A.; Xu, Y.; Cai, S.; Yang, W. New Application of Old Material: Chinese Traditional Ink for Photothermal Therapy of Metastatic Lymph Nodes. *ACS Omega* **2017**, *2*, 5170−5178.
(44) Blázquez-Castro, A.; Colombo, L. L.; Vanzulli, S. I.; Stockert, J. C. NIR Laser Pointer for in Vivo Photothermal Therapy of Murine LM3 Tumor Using Intratumoral China Ink as a Photothermal Agent. *Lasers Med. Sci.* **2018**, *33*, 1307−1315.
(45) Cai, Y.; Si, W.; Huang, W.; Chen, P.; Shao, J.; Dong, X. Organic Dye Based Nanoparticles for Cancer Phototheranostics. *Small* **2018**, *14*, 1704247.
(46) Lee, K. Y.; Mooney, D. J. Alginate: Properties and Biomedical Applications. *Prog. Polym. Sci.* **2012**, *37*, 106−126.
(47) Pan, H.; Zhang, C.; Wang, T.; Chen, J.; Sun, S.-K. In Situ Fabrication of Intelligent Photothermal Indocyanine Green-Alginate Hydrogel for Localized Tumor Ablation. *ACS Appl. Mater. Interfaces* **2019**, *11*, 2782−2789.
(48) Zhang, J.; Zhang, J.; Li, W.; Chen, R.; Zhang, Z.; Zhang, W.; Tang, Y.; Chen, X.; Liu, G.; Lee, C.-S. Degradable Hollow Mesoporous Silicon/Carbon Nanoparticles for Photoacoustic Imaging-Guided Highly Effective Chemo-Thermal Tumor Therapy in Vitro and in Vivo. *Theranostics* **2017**, *7*, 3007−3020.
(49) Tang, Z.; Zhang, H.; Liu, Y.; Ni, D.; Zhang, H.; Zhang, J.; Yao, Z.; He, M.; Shi, J.; Bu, W. Antiferromagnetic Pyrite as the Tumor Microenvironment-Mediated Nanoplatform for Self-Enhanced Tumor Imaging and Therapy. *Adv. Mater.* **2017**, *29*, 1701683.
(50) Lee, S.-H.; Tang, C.-H.; Lin, W.-Y.; Chen, K.-H.; Liang, H.-J.; Cheng, T.-J.; Lin, C.-Y. LC-MS-based Lipidomics to Examine Acute Rat Pulmonary Responses After Nano- and Fine-Sized ZnO Particle Inhalation Exposure. *Nanotoxicology* **2018**, *12*, 439−452.
(51) Triebl, A.; Trötzmüller, M.; Hartler, J.; Stojakovic, T.; Köfeler, H. C. Lipidomics by Ultrahigh Performance Liquid Chromatography-High Resolution Mass Spectrometry and its Application to Complex Biological Samples. *J. Chromatogr. B: Anal. Technol. Biomed. Life Sci.* **2017**, *1053*, 72−80.
(52) Zhang, Z.-H.; Vaziri, N. D.; Wei, F.; Cheng, X.; Bai, X.; Zhao, Y. An Integrated Lipidomics and Metabolomics Reveal Nephroprotective Effect and Biochemical Mechanism of Rheum Officinale in Chronic Renal Failure. *Sci. Rep.* **2016**, *6*, 22151.
(53) Dong, Z.; Feng, L.; Chao, Y.; Hao, Y.; Chen, M.; Gong, F.; Han, X.; Zhang, R.; Cheng, L.; Liu, Z. Amplification of Tumor Oxidative Stresses with Liposomal Fenton Catalyst and Glutathione Inhibitor for Enhanced Cancer Chemotherapy and Radiotherapy. *Nano Lett.* **2019**, *19*, 805−815.
(54) Hayashi, K.; Sakamoto, W.; Yogo, T. Smart Ferrofluid with Quick Gel Transformation in Tumors for MRI-Guided Local Magnetic Thermochemotherapy. *Adv. Funct. Mater.* **2016**, *26*, 1708−1718.
(55) Chao, Y.; Xu, L.; Liang, C.; Feng, L.; Xu, J.; Dong, Z.; Tian, L.; Yi, X.; Yang, K.; Liu, Z. Combined Local Immunostimulatory Radioisotope Therapy and Systemic Immune Checkpoint Blockade Imparts Potent Antitumour Responses. *Nat. Biomed. Eng.* **2018**, *2*, 611−621.
(56) Peppas, N.; Bures, P.; Leobandung, W.; Ichikawa, H. Hydrogels in Pharmaceutical Formulations. *Eur. J. Pharm. Biopharm.* **2000**, *50*, 27−46.
(57) Zheng, D.-W.; Li, B.; Li, C.-X.; Xu, L.; Fan, J.-X.; Lei, Q.; Zhang, X.-Z. Photocatalyzing CO_2 to CO for Enhanced Cancer Therapy. *Adv. Mater.* **2017**, *29*, 1703822.
(58) Lin, L.-S.; Huang, T.; Song, J.; Ou, X.-Y.; Wang, Z.; Deng, H.; Tian, R.; Liu, Y.; Wang, J.-F.; Liu, Y.; Yu, G.; Zhou, Z.; Wang, S.; Niu, G.; Yang, H.-H.; Chen, X. Synthesis of Copper Peroxide Nanodots for H_2O_2 Self-Supplying Chemodynamic Therapy. *J. Am. Chem. Soc.* **2019**, *141*, 9937−9945.
(59) Yang, W. S.; Kim, K. J.; Gaschler, M. M.; Patel, M.; Shchepinov, M. S.; Stockwell, B. R. Peroxidation of Polyunsaturated Fatty Acids by Lipoxygenases Drives Ferroptosis. *Proc. Natl. Acad. Sci. U.S.A.* **2016**, *113*, E4966−E4975.
(60) Stockwell, B. R.; Friedmann Angeli, J. P.; Bayir, H.; Bush, A. I.; Conrad, M.; Dixon, S. J.; Fulda, S.; Gascón, S.; Hatzios, S. K.; Kagan, V. E.; Noel, K.; Jiang, X.; Linkermann, A.; Murphy, M. E.;

DOI: 10.1021/acsami.9b15009
ACS Appl. Mater. Interfaces 2019, 11, 38555−38567

Overholtzer, M.; Oyagi, A.; Pagnussat, G. C.; Park, J.; Ran, Q.; Rosenfeld, C. S.; Salnikow, K.; Tang, D.; Torti, F. M.; Torti, S. V.; Toyokuni, S.; Woerpel, K. A.; Zhang, D. D. Ferroptosis: A Regulated Cell Death Nexus Linking Metabolism, Redox Biology, and Disease. *Cell* **2017**, *171*, 273−285.

DOI: 10.1021/acsami.9b15009
ACS Appl. Mater. Interfaces 2019, 11, 38555−38567